

# High-Efficiency Broadband Meta-Hologram with Polarization-Controlled Dual Images

Wei Ting Chen,<sup>†,▲</sup> Kuang-Yu Yang,<sup>‡,▲</sup> Chih-Ming Wang,<sup>\*,§,▲</sup> Yao-Wei Huang,<sup>†</sup> Greg Sun,<sup>||</sup> I-Da Chiang,<sup>⊥</sup> Chun Yen Liao,<sup>†</sup> Wei-Lun Hsu,<sup>⊥</sup> Hao Tsun Lin,<sup>⊥</sup> Shulin Sun,<sup>||</sup> Lei Zhou,<sup>#</sup> Ai Qun Liu,<sup>●</sup> and Din Ping Tsai<sup>\*,†,‡,⊥</sup>

<sup>†</sup>Graduate Institute of Applied Physics, National Taiwan University, Taipei 10617, Taiwan

<sup>‡</sup>Research Center for Applied Sciences, Academia Sinica, Taipei 115, Taiwan

<sup>§</sup>Institute of Opto-electronic Engineering, National Dong Hwa University, Hualien 97401, Taiwan

<sup>||</sup>Department of Physics, University of Massachusetts Boston, Boston, Massachusetts 02125, United States

<sup>⊥</sup>Department of Physics, National Taiwan University, Taipei 10617, Taiwan

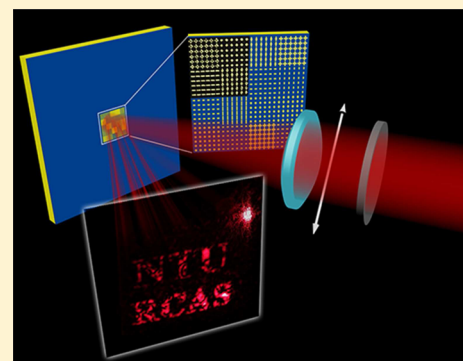
<sup>||</sup>Department of Optical Science and Engineering and <sup>#</sup>State Key Laboratory of Surface Physics and Key Laboratory of Micro and Nano Photonic Structures (Ministry of Education), Fudan University, Shanghai 200433, China

<sup>●</sup>School of Electrical and Electronic Engineering, Nanyang Technological University, Singapore 639798, Singapore

## S Supporting Information

**ABSTRACT:** Holograms, the optical devices to reconstruct predesigned images, show many applications in our daily life. However, applications of hologram are still limited by the constituent materials and therefore their working range is trapped at a particular electromagnetic region. In recent years, the metasurfaces, an array of subwavelength antenna with varying sizes, show the abilities to manipulate the phase of incident electromagnetic wave from visible to microwave frequencies. Here, we present a reflective-type and high-efficiency meta-hologram fabricated by metasurface for visible wavelength. Using gold cross nanoantennas as building blocks to construct our meta-hologram devices with thickness  $\sim \lambda/4$ , the reconstructed images of meta-hologram show polarization-controlled dual images with high contrast, functioning for both coherent and incoherent light sources within a broad spectral range and under a wide range of incidence angles. The flexibility demonstrated here for our meta-hologram paves the road to a wide range of applications related to holographic images at arbitrary electromagnetic wave region.

**KEYWORDS:** Metasurfaces, meta-hologram, reflection phase, cross nanoantennas, polarization-controlled dual images



Holograms, the optical devices to reconstruct predesigned images, have been advanced dramatically with the development of today's nanotechnology.<sup>1–3</sup> However, applications of holograms are still limited by the constituent materials, and their working range is rather narrow. On the other hand, metamaterials<sup>4,5</sup> artificially constructed with subwavelength structures have significantly expanded the variation range of refraction index, allowing for far more functionalities and broader operating range than those optical devices made of materials that exist in nature. However, previous efforts in making transmittive holograms with bulky metamaterials suffered low efficiencies for image constructions, since light has to travel through the structured metal layers for phase accumulation so that strong light absorption is inevitable.<sup>4,5</sup>

Metamaterials classified as artificial materials possessing properties that do not exist in nature have been the subject of hot pursuits in recent years.<sup>6–10</sup> The rapid advancement in nanofabrication technology has continuously been fueling the research efforts in stimulating ideas and realizing designs of

more advanced and functional optical devices. The driving principle behind these efforts is the ability to achieve nearly arbitrary effective indices that span over the range of those of constituent materials that are selected to construct the metamaterials. As a result, optical metamaterials can have spatial refractive index contrasts that are orders of magnitude greater than what have been realized with in dielectric media as well as in polymers.<sup>11–13</sup> One particular element that shows up in nearly all optical metamaterials is metal because it naturally forms a huge dielectric contrast with its hosting dielectric medium and a small subwavelength metal structure possesses a large electric dipole that effectively couples with electromagnetic (EM) waves. Indeed, a key feature of these metamaterials (referred to here as plasmonic metamaterials) is the inclusion of subwavelength metal structures typically in

**Received:** October 11, 2013

**Revised:** December 6, 2013

the nanometer scale arranged in particular spatial patterns that allow for the use of effective medium approach to describe their EM response in phase and amplitude sensitive to both shape and orientation of the metal nanostructures, exhibiting spectral resonance. Such a property has been a pillar element in a variety of optical devices made of plasmonic metamaterials. Very recently, a phase holographic device made of a metamaterial medium consisting of multilayer, subwavelength, metal structures has been demonstrated in the far-infrared.<sup>14</sup> A first of its kind ever produced with a metamaterial with layers of metal structures, the device suffered from significant metal absorption and generated holographic images of very low efficiency. As a matter of fact, this is not unique to this particular optical application, rather a very significant trade-off that all plasmonic metamaterials have to contend with when operating in the optical frequencies.

Here we present a phase hologram based on a subcategory of metamaterials, namely metasurfaces, that form much brighter images with higher efficiencies in the visible range. Metasurfaces as the two-dimensional (2D) version of metamaterials are constructed with subwavelength metal structures of various dimensions and shapes with the ability to modulate the EM waves from microwave, infrared to visible region.<sup>15–18</sup> While both phase and amplitude of light can be modulated by tuning the geometric parameters of a metasurface, only phase modulation is preferred for a high-efficiency meta-hologram because the modulation of amplitude is typically the result of metal absorption that always leads to low diffraction efficiency and should be avoided. In comparison with conventional optical devices that rely on the spatial variation of the refractive index, plasmonic metasurfaces have both their thicknesses and pixel sizes or unit cells much smaller than the incident wavelengths. For instance, human eye, a typical gradient index element, has the refractive index  $n \sim 1.406$  in the central part and  $n \sim 1.386$  around the edge. Because the refraction index variation is small  $\Delta n \sim 0.02$ , it needs enough thickness ( $\sim 5$  mm) for phase accumulation to form images with good resolution and focusing on human retina.<sup>19</sup> The thickness of diffractive optical devices such as gratings and Fresnel lens are usually comparable to the wavelength of incident wave. The spatial light modulator (SLM) that has been used in holographic data storage and display typically has pixel size on the order of  $\sim 10$   $\mu\text{m}$ . In addition, the thinner metasurfaces capable of controlling the phase of light transmitting or reflecting from a 2D array of metal nanostructures of adjusted dimensions and orientations offer the benefit of reduced metal absorption relative to those 3D multilayer metamaterials, and for those applications where substantial light penetration inside the bulk of metamaterials can be avoided, such as the reflective hologram, metasurfaces have significant advantages. Introducing plasmonic metasurface into holography removes the limitations on traditional or even the more recent digital holograms based on either emulsions or photopolymers as recording media that oftentimes restrict the light source for image reconstruction to be at a single wavelength, because metal nanostructures have the ability to modulate the phase of incident wave over a wide frequency range. The high-efficiency hologram presented here uses a metasurface as a phase modulator to generate reflective hologram (Figure 1) rather than the transmitting image that was formed with light propagating through four layers of metal structures.<sup>14</sup> With our advanced e-beam lithography, the feature size of the metal structures has been substantially reduced to

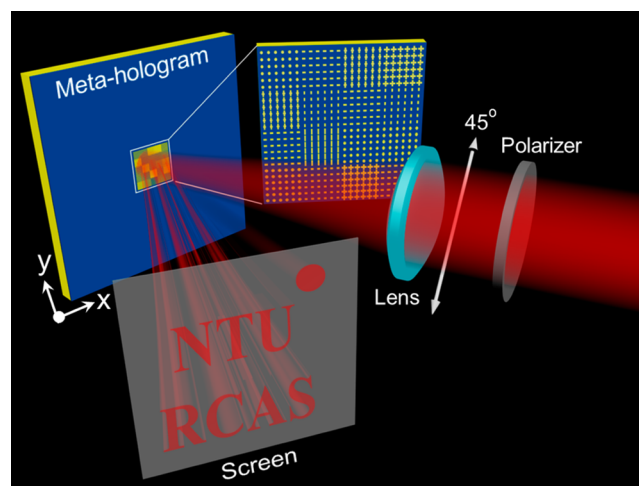


**Figure 1.** Illustration of our designed meta-hologram under  $45^\circ$  linearly polarized illumination. The phase distributions of the two images, RCAS and NTU, were recorded on the meta-hologram sample by e-beam lithography. Pixels of  $6 \times 6$  gold cross nanoantennas of various sizes were patterned on a 50 nm thick  $\text{MgF}_2$  spacer sputtered on a gold mirror. The images NTU and RCAS can be reconstructed by linearly polarized light along the  $x$ - or  $y$ -direction, respectively, with a broadband light source over a broad incident angle.

shift our device to operate in the visible range. The metasurface is constructed simply with metal nanorods of equal thickness and width but varied lengths. Utilizing the localized surface plasmon (LSP) resonance selectivity on light polarization by the metal rods, we are able to simultaneously encode two holograms on the same metasurface and each image is reconstructed with an incident light with polarization perpendicular to the other.

Figure 1 shows the schematic setup of our meta-hologram under  $45^\circ$  linearly polarized illumination that reconstructs both holographic images “NTU” and “RCAS”. We designed the metasurface using the principle of computer-generated hologram (CGH) method.<sup>20</sup> The basic elements on the metasurface are gold nanorods of different length, but all with the same 50 nm thick and 60 nm width (inset in Figure 2a) patterned on top of a 50 nm thick  $\text{MgF}_2$  on a 130 nm thick gold mirror. Each nanorod behaves as a nanoantenna and their long axes are aligned in the direction of incident wave polarization; under illumination the strong LSP resonance accompanied with dramatic phase modulation of reflected electromagnetic wave is excited through the antiparallel electric current oscillation on the nanoantennas and gold mirror where the phase of reflected wave can be engineered independently by varying the length of the nanorod. We have performed finite-difference time-domain (FDTD) simulations to calculate phase modulation and reflectance of periodic gold nanorods, and the results are shown in Figure 2a as a function of rod length under the normal incidence of a plane wave at  $\lambda = 780$  nm with polarization along the long axis of rod where each nanorod occupies a  $250 \times 250$  nm<sup>2</sup> square (inset in Figure 2a). The reflectance and phase distributions as a function of the length of the nanorod and the wavelength are shown in Supporting Information Figure S1. It can be seen that nanorods with lengths around 110 nm have their LSP resonance at  $\lambda = 780$  nm. From the phase modulation curve, we selected four values of length ( $L = 60, 105, 125$ , and  $209$  nm) corresponding to the reflection phase separated by  $90^\circ$  to design a 4-level phase

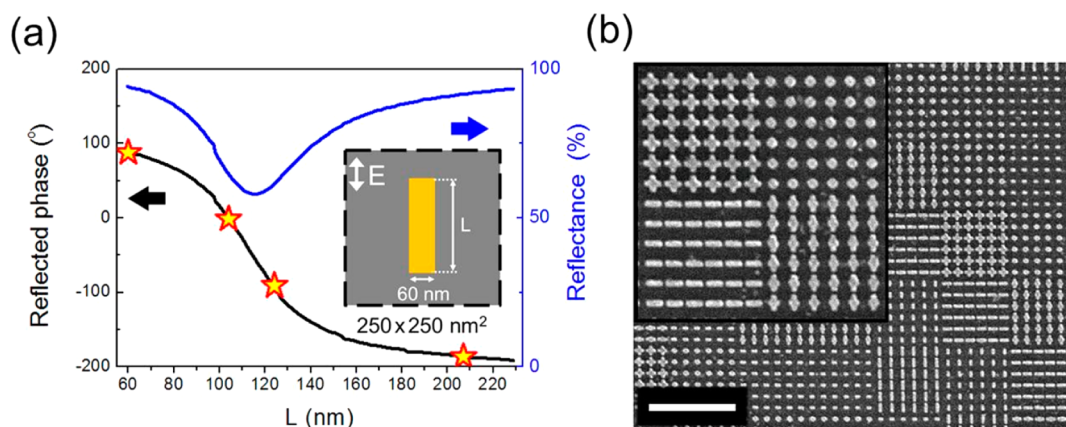


**Figure 2.** (a) Reflected phase and reflectance versus the length of Au nanorods arranged periodically in a unit cell of  $250 \times 250 \text{ nm}^2$  on top of a 50 nm  $\text{MgF}_2$  spacer sputtered on a 130 nm Au ground plate under the illumination of 780 nm light at normal incidence polarized along the nanorod length. Four nanorod lengths ( $L = 60, 105, 125$ , and  $209 \text{ nm}$ ) with phase separation of  $\pi/2$  were chosen to construct the phase pixels of the meta-hologram sample, (b) SEM image of the meta-hologram sample and the inset with higher magnification. The scale bar is  $2 \mu\text{m}$ .

plasmonic meta-hologram. While the holographic image is reconstructed with the phase modulation induced by the different sizes of the metal bars from pixel to pixel, the same size variation also causes the unintended amplitude modulation. The average reflectance of the four selected nanorods is about  $\sim 80\%$  with the gold Ohmic loss taken into account, which is the reason for the high efficiency holographic images that we have observed. We obtain the phase distribution by taking iterative Fourier transform of both images NTU and RCAS (see meta-hologram design in Supporting Information for details). The phase distribution is then digitized with the phase pixels, each of which occupying a total area of  $1500 \times 1500 \text{ nm}^2$  is constructed with  $6 \times 6$  gold nanorods of a fixed length that approximates the required phase on the 2D metasurface for a particular image. In order for them to be reconstructed with incident waves with perpendicular polarizations, the pixel arrays of the two images are turned  $90^\circ$  to each other. The spatial overlapping of the pixels for the different images therefore forms  $6 \times 6$  nanocrosses (Figure 2b). There are 16 different nanocross pixels distributed on the meta-hologram sample because of the 16 combinations with 4 different-length gold nanorods for each image. The meta-hologram sample was fabricated with standard e-beam lithography, consisting of  $100 \times 100$  pixels. Figure 2b shows the scanning electron microscope (SEM) image of a small region of the fabricated sample (optical image of fabricated sample is shown in Supporting Information Figure S3).

Optical measurement setup shown in Figure 3a is used to characterize the performance of the fabricated meta-hologram. We used several light sources to characterize the performance of the plasmonic meta-hologram, including laser diodes emitting at different wavelengths (780, 640, 632.8, 488, and 405 nm) and a lamp with or without filter (see meta-hologram measurement in Supporting Information for details). The meta-hologram sample is mounted on a rotation stage, allowing adjustment the incident angle. Three far-field diffractive images of the meta-hologram under  $x$ -,  $45^\circ$ - and  $y$ -polarized incidence with  $\theta = 15^\circ$  using the 780 nm laser diode are shown in Figure 3b–d (see Figure S4 for the images with  $\theta > 15^\circ$ ). As the laser beam polarization being rotated from  $x$ - to  $y$ -direction, the projected patterns smoothly transitioned from NTU to RCAS, and the intensities of the two nonoverlapping patterns rise and fall according to the degree of polarization alignment with

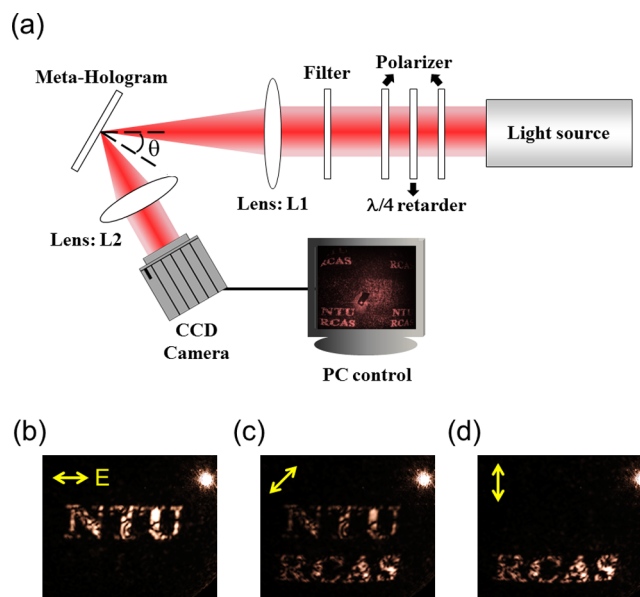


**Figure 3.** (a) The measurement setup for the reconstruction of the holographic images. The filter, polarizers and  $\lambda/4$  retarder are selectively used. The reconstructed image under (b)  $x$ -polarized, (c)  $45^\circ$ -polarized, and (d)  $y$ -polarized using the 780 nm laser with the incident angle  $\theta = 15^\circ$ .

either  $x$ - or  $y$ -direction (see Supporting Information Supplementary Movie), which is in excellent agreement with our design. The measured polarization contrast is  $\sim 18$  obtained as the ratio of the average intensity in the region of characters NTU to that of RCAS in the case of  $x$ -polarized illumination, confirming the polarization-selective ability of our device. Furthermore, the images collected as the first order diffraction patterns can be clearly resolved in the same display screen with the zero-order diffraction spot at the upper right corner, indicating the high efficiency of the reflective meta-hologram. We shall use the definition for efficiency as

$$\text{Efficiency} = \frac{P_{\text{NTU}}}{P_{\text{laser}}}$$

where  $P_{\text{NTU}}$  is the average optical power of the first-order NTU image (measured before focus lens L2) and  $P_{\text{laser}}$  is that of the



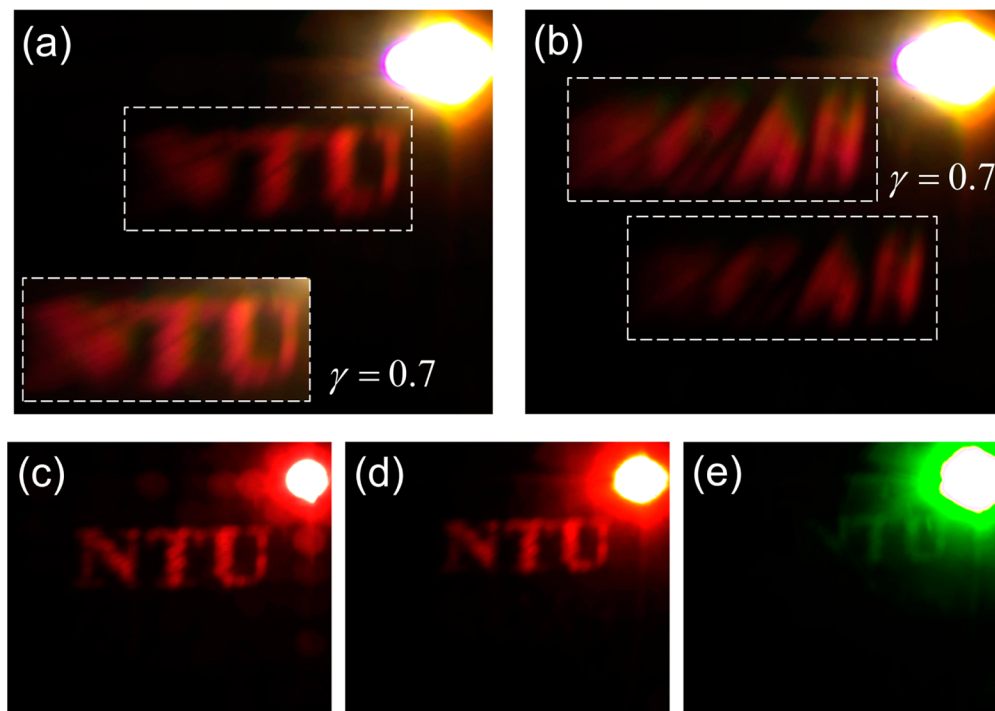


**Figure 4.** Reconstructed images of meta-hologram using a broadband incoherent light source spanning the spectral range of visible and near-infrared at the incident angle  $\theta = 15^\circ$ . (a,b) Images generated under  $x$ - and  $y$ -polarized illumination, respectively. (c–e) Images under  $x$ -polarized illumination obtained by applying bandpass filters with pass region  $\lambda = 700 \pm 20$ ,  $600 \pm 20$ , and  $550 \pm 20$  nm, respectively.

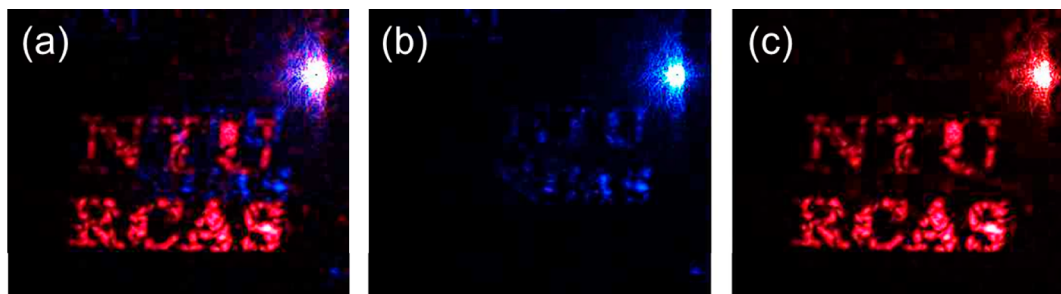


**Figure 5.** Meta-hologram images reconstructed using a dual wavelength (488 and 640 nm) laser diode system at  $45^\circ$  polarization and incident angle  $\theta = 15^\circ$ . The two laser beams are coaxially illuminated at the same point on the sample, and the laser powers are 0.1 and 0.02 mW at 488 and 640 nm, respectively. The images are produced under (a) both 488 and 640 nm laser beams, (b) only 488 nm laser, and (c) only 640 nm laser.

$x$ -polarized incident beam (measured before focus lens L1). We measured the power of the first-order NTU image by placing a lens at the location of the image to focus the diffraction light into a photodiode. Diffraction efficiency of 18% was recorded with the 780 nm laser diode at the angle of incidence  $\theta = 15^\circ$ .

While the meta-hologram is designed to operate at 780 nm wavelength, we also measured its functionality using a broadband incoherent source since the LSP resonance typically exhibits broad spectral features. Indeed the images NTU and RCAS can be reconstructed with a broadband incoherent light source (LDLS EQ-99FC from ENERGETIQ, see Supporting Information Figure S2 for its typical spectrum) coupled with a multimode optical fiber (1 mm core diameter P1000-2-VIS-NIR from ocean optics) that is equipped with a collimated lens (74 UV from ocean optics). Figure 4a,b shows the images of NTU and RCAS taken by a CCD camera (sCMOS pco.edge) under  $x$ - and  $y$ -polarized incoherent light illumination, respectively, using gamma correction  $\gamma = 0.7$  for optimal visual clarity. Unlike the images produced by the coherent laser beam, the reconstructed letters here are without speckles, but the

projected patterns are more blurred because of the chromatic dispersion induced by the broadband light source. Figure 4c–e are the “NTU” images obtained by applying a bandpass filter with pass regions at  $\lambda = 700 \pm 20$ ,  $600 \pm 20$ , and  $550 \pm 20$  nm, respectively, to allow for a close examination of the images reconstructed with illuminations at specific wavelengths. The image obtained with the  $550 \pm 20$  nm bandpass filter in Figure 4e appears to have the lowest efficiency because of the higher absorption loss for gold at this shorter wavelength region. Nevertheless, the broadband functionality of the meta-hologram is clearly demonstrated.

We have also conducted image-reconstruction using a dual-wavelength laser diode system (488 and 640 nm) that enabled us to reconstruct the image under different wavelength illumination without having to readjust the optical setup. Figure 5a presents the images simultaneously illuminated by the two coaxial laser beams ( $\lambda = 488$  nm and  $\lambda = 640$  nm) that are both linearly polarized near  $45^\circ$  such that both NTU and RCAS are reconstructed. The power of 488 and 640 nm diode lasers are attenuated to around 0.1 and 0.02 mW, respectively. It can

be clearly observed that the blue patterns at 488 nm are positioned closer to the zero-order diffraction spot located at the upper right corner and with a smaller scale compared to that of the red one at 640 nm. In addition, the efficiency of pattern reconstructed by the 488 nm laser is significantly depressed because of the stronger gold absorption loss in this region. Figure 5b,c shows the images reconstructed individually by the 488 and 640 nm lasers (see Supporting Information Supplementary Movie for switching wavelength).

We subsequently studied the hologram efficiency as a function of the incident angle of the illumination. We experimentally measured the efficiencies of the meta-hologram illuminated by three laser diodes at  $\lambda = 780, 632.8,$  and  $405$  nm by varying their incident angles  $\theta$  and the results are shown in Figure 6 (the optical images of different incident angle  $\theta$  under

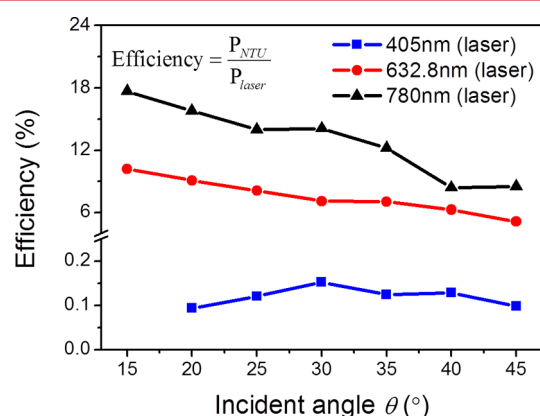


**Figure 6.** Meta-hologram efficiency versus incident angle  $\theta$  at 780, 632.8, and 405 nm incident wavelengths, which is defined as the ratio of the power of image divided by the power of laser beam before passing through the focusing lens.

780 nm laser illumination is attached in Supporting Information Figure S4). The efficiency obtained with the 780 nm laser is the highest throughout the measured incident angle range because the meta-hologram sample is designed and therefore better optimized at this wavelength. At  $15^\circ$  incidence, the efficiency reaches 18% for 780 nm illumination and reduces to  $\sim 10\%$  for 632.8 nm and is essentially unmeasurable for 405 nm illumination because of the significant metal loss. With the increase of the incident angle, the efficiencies for both 780 and 632.8 nm showed a decreasing trend, while that of the 405 nm case remains consistently low at around 0.1%. It should be pointed out that the efficiencies only drop down to 8.5 and 5.1% for 780 and 632.8 nm illuminations, respectively, at  $45^\circ$  incident angle.

In comparison with prior plasmonic metamaterial approaches, our meta-hologram scheme employing reflectance to reconstruct the images is far more efficient; our best efficiency reached 18% versus those of  $<1\%$  that were obtained either theoretically or experimentally.<sup>14,21,22</sup> Our meta-hologram also exhibits broadband characteristic with a bandwidth of  $\sim 880$  nm, according to our numerical and theoretical calculation (see Figure S5 in Supporting Information for detailed discussion). Furthermore, our meta-hologram work still shows higher efficiency and greater polarization contrast under oblique incoherent illumination than those using dielectric materials such as Si nanoantenna,<sup>23</sup> SiO<sub>2</sub> subwavelength structures,<sup>24</sup> and carbon nanotubes.<sup>25</sup>

To summarize, we have proposed and demonstrated plasmonic meta-hologram with significantly higher efficiencies than what have been designed and achieved so far using metamaterials. The reflective hologram approach allows us to employ plasmonic metasurface as a 2D structure that has a number of advantages such as simple fabrication process, low metal absorption, broad working spectral range, and greater tolerance to variation of incident angle and light incoherence. The meta-hologram sample consists of pixels made of  $6 \times 6$  cross nanoantennas of 16 different shapes for the phase modulation that yields polarization-controlled dual images. A four phase level design has been implemented for the e-beam lithography to pattern those cross nanoantennas. We believe the efficiency can be further improved by increasing the phase levels of the meta-hologram, namely using more different lengths of the gold nanorods for more phases. The polarization-controlled dual images of meta-hologram have potential applications in performing glass-free 3D imaging<sup>26</sup> and data storage.<sup>27–29</sup> Finally, by combining with the techniques of tunable metamaterials,<sup>30</sup> meta-hologram can potentially be used to realize active hologram that works at arbitrary frequency.

## ■ ASSOCIATED CONTENT

### § Supporting Information

Detailed information of meta-hologram design, fabrication, measurement, optical images of fabricated meta-hologram and reconstructed CCD images for different incident angles  $\theta$ , and meta-hologram efficiency analysis. This material is available free of charge via the Internet at <http://pubs.acs.org>.

## ■ AUTHOR INFORMATION

### Corresponding Authors

\*(D.P.T.) E-mail: [dptsai@phys.ntu.edu.tw](mailto:dptsai@phys.ntu.edu.tw).

\*(C.-M.W.) E-mail: [wangcm@mail.ndhu.edu.tw](mailto:wangcm@mail.ndhu.edu.tw).

### Author Contributions

▲W.T.C., K.-Y.Y., and C.-M.W. contributed equally to this work.

### Notes

The authors declare no competing financial interests.

## ■ ACKNOWLEDGMENTS

The authors would like to thank the National Science Council of Taiwan (Contract Nos. NSC102-2745-M-002-005-ASP and NSC102-2911-I-002-505) for financial support. L.Z. thanks financial supports from the National Science Foundation of China (60990321, 11174055) and the Program of Shanghai Subject Chief Scientist (12XD1400700).

## ■ REFERENCES

- (1) Gabor, D. *Nature* **1948**, *161*, 777–778.
- (2) Ozaki, M.; Kato, J.-i.; Kawata, S. *Science* **2011**, *332*, 218–220.
- (3) Blanche, P. A.; et al. *Nature* **2010**, *468*, 80–83.
- (4) Chen, W. T.; et al. *Opt. Express* **2011**, *19*, 12837–12842.
- (5) Soukoulis, C. M.; Wegener, M. *Nat. Photonics* **2011**, *5*, 523–530.
- (6) Chen, X. Z.; et al. *Nat. Commun.* **2012**, *3*, 1198.
- (7) Zhu, W. M.; et al. *Nat. Commun.* **2012**, *3*, 1274.
- (8) Ren, M.; Plum, E.; Xu, J.; Zheludev, N. I. *Nat. Commun* **2012**, *3*, 833.
- (9) Yang, Y.; et al. *Nat. Commun* **2012**, *3*, 651.
- (10) Chen, W. T.; et al. *Appl. Phys. Lett.* **2011**, *98*, 171106.
- (11) Yakhkind, A. K. *J. Opt. Technol.* **2001**, *70*, 877–881.
- (12) Jin, Y.; Tai, H.; Hiltner, A.; Baer, E.; Shirk, J. S. *J. Appl. Polym. Sci.* **2007**, *103*, 1834–1841.

- (13) Glezer, E. N.; et al. *Opt. Lett.* **1996**, *21*, 2023–2025.
- (14) Larouche, S.; Tsai, Y. J.; Tyler, T.; Jokerst, N. M.; Smith, D. R. *Nat. Mater.* **2012**, *11*, 450–454.
- (15) Sun, S. L.; et al. *Nat. Mater.* **2012**, *11*, 426–431.
- (16) Sun, S. L.; et al. *Nano Lett.* **2012**, *12*, 6223–6229.
- (17) Ni, X. J.; Emani, N. K.; Kildishev, A. V.; Boltasseva, A.; Shalaev, V. M. *Science* **2012**, *335*, 427–427.
- (18) Yu, N.; et al. *Science* **2011**, *334*, 333–337.
- (19) Hecht, E. *Optics*, Addison Wesley series in physics; DA Information Services: Mitcham, VIC, 2002; Vol. 4, p 208.
- (20) Wyrowski, F.; Bryngdahl, O. *J. Opt. Soc. Am. A* **1988**, *5*, 1058–1065.
- (21) Walther, B.; et al. *Adv. Mater.* **2012**, *24*, 6300–6304.
- (22) Zhou, F.; Liu, Y.; Cai, W. P. *Opt. Express* **2013**, *12*, 4348–4354.
- (23) Sun, J.; Timurdogan, E.; Yaacobi, A.; Hosseini, E. S.; Watts, M. R. *Nature* **2013**, *493*, 195–199.
- (24) Yu, W.; et al. *Appl. Opt.* **2002**, *41*, 96–100.
- (25) Butt, H.; et al. *Adv. Mater.* **2012**, *24*, OP331–OP336.
- (26) Dodgson, N. A. *Nature* **2013**, *495*, 316–317.
- (27) Graham-Rowe, D. *Nat. Photonics* **2007**, *1*, 197–200.
- (28) Buse, K.; Adibi, A.; Psaltis, D. *Nature* **1998**, *393*, 665–668.
- (29) Heanue, J. F.; Bashaw, M. C.; Hesselink, L. *Science* **1994**, *265*, 749–752.
- (30) Ou, J.-Y.; Plum, E.; Zhang, J.; Zheludev, N. I. *Nat. Nanotechnol.* **2013**, *8*, 252–255.